Millimeter-Wave Characterization of Dielectric Materials Using Calibrated FMCW Transceivers

Jan Barowski, *Member, IEEE*, Marc Zimmermanns, and Ilona Rolfes, *Member, IEEE*

***Abstract*— This paper presents a measurement setup, an extraction algorithm, and the results from material characterization measurements in the millimeter-wave (mm-wave) regime using ultrawideband frequency-modulated continuous-wave (FMCW) radar transceivers. The complex permittivity of dielectric and nonmagnetic materials is derived from radar echoes using a high-gain dielectric lens antenna setup and a measurement setup comprising elliptic mirrors. The radar transceivers perform fast and accurate measurements from 200 to 250 GHz within milliseconds. The FMCW transceivers are calibrated using a frequency-domain model that describes the systematic errors in the measurement setup. The characterization is done by a holistic model-based approach. Several well-known dielectric materials, such as polytetrafluorethylene, polyvinylchloride (PVC), or acrylic glass, are characterized among others to validate the setup's accuracy. The characterization is also done for different samples of polylactide, which is commonly used in additive manufacturing processes and 3-D printing, making it of high interest for the construction of mm-wave components.**

***Index Terms*— Calibration techniques, electromagnetic simulation, material characterization, millimeter wave (mm-wave) and submillimeter waves, radar systems.**

I. Introduction

RADAR transceivers based on the frequency-modulated continuous-wave (FMCW) principle are very well-known for their military but also civil applications in the fields of ranging, imaging, and target detection as well as identification. The vast field of industrial process monitoring using FMCW sensors comprises tank-level probing [1], flow measurements [2], and tomographic measurements [3], among others. In these applications, radar-based systems are advantageous in comparison with vector network analyzers (VNAs), since they can be realized at a high level of compactness and are much cheaper than laboratory equipment. Whereas the aforementioned measurement tasks depend more strongly on the dynamic range and contrast with the measurement result [4], [5], material characterization tasks are usually need to be performed with absolute exactness of the reflection magnitude and phase [6]. This is of special importance when free-space measurements are done, since the wave propagation from the antenna to the material under test (MUT) results in additional phase rotation and attenuation, which is hardly identified without further calibration measurements [7]. Usually, such measurements are carried out using VNA setups that utilize the built-in opportunity for calibrating the VNA based on three or more calibration measurements with fully or partially known calibration standards [8]. Even though FMCW radar systems are performing a time-domain measurement, their special chirp-pulse allows for a frequency-domain description of the radar transceiver very similar to a VNA. Recently, this method was applied to millimeter-wave (mm-wave) radar measurements [9] and measurements with orthogonal incidence [10] on the MUT. Up to now, the measurement setup utilized high-gain dielectric lenses resulting in plane-wave fronts [10], whereas even higher accuracies can be achieved using focusing setups based on elliptic mirrors, as will be shown in this contribution.

Based on the frequency-domain error model, a calibration method for FMCW transceivers is presented in Section II. The calibration approach also reflects on the special properties of the intermediate frequency (IF) signal of the measurement device, which is not fully equivalent to a complex signal obtained by a VNA measurement. In Section III, both the measurement setups and the execution of the calibration measurements are explained. Wave propagation and focusing in both the setups are analyzed by a full-wave simulation of the antennas, lenses, and mirrors. Based on additional measurements of the calibration standards, this section also offers an estimation of the measurement's dynamic range. The algorithm used for the extraction of the relative permittivity as well as the dielectric losses is presented in Section IV. The proposed method utilizes a model-based approach in combination with an iterative method to match the reflection factor obtained from the measurement to the expected analytic one. Section V discusses the material characterization results obtained from several samples of well-documented materials and also other materials of interest to mm-wave applications. These include reflection factor measurements for materials in future communication scenarios as well as additive manufacturing materials at different fill rates. A conclusion

Manuscript received January 3, 2018; revised June 11, 2018; accepted June 21, 2018. Date of publication July 30, 2018; date of current version August 6, 2018. This work was supported by the Deutsche Forschungsgemeinschaft within the frame of SFB-TRR 196. This paper is an expanded version from the IEEE MTT-S International Microwave Workshop Series on Advanced Materials and Processes (IMWS-AMP 2017), Pavia, Italy, September 20–22, 2017. *(Corresponding author: Jan Barowski.)*

The authors are with the Department of Electrical Engineering and Information Technologies, Institute of Microwave Systems, Ruhr University Bochum, 44801 Bochum, Germany (e-mail: jan.barowski@rub.de; marc.zimmermanns@rub.de; ilona.rolfes@rub.de).

Color versions of one or more of the figures in this paper are available online at http://ieeexplore.ieee.org.

Digital Object Identifier 10.1109/TMTT.2018.2854180

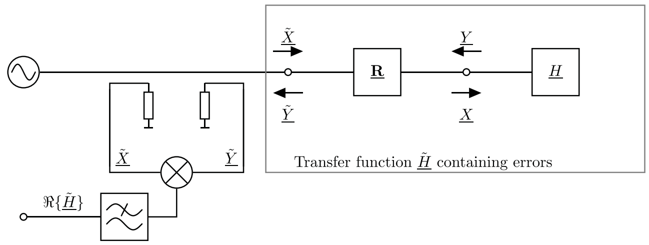

Fig. 1. Systematic view of the FMCW transceiver as a 1-port reflectometer containing the error network $\underline{\mathbf{R}}$.

of the contribution and a summarizing discussion is given in Section VI.

II. System Model and Calibration

The calibration of the FMCW device is done in the frequency domain, considering the measurement system as a 1-port reflectometer, which is also shown in Fig. 1. This interpretation of the radar sensor is based on [11].

A. System Description

The IF signal is captured by an ideal sensor on the left-hand side of Fig. 1. From the theory of FMCW systems, it can be shown that the time-domain IF signal $S(t)$ is equivalent to the real part of the measured transfer function $\underline{H}(j\omega(t))$ in the frequency domain. The equivalence originates from the linear frequency chirp

$$\omega(t) = \omega_0 + \frac{\Omega \cdot t}{T} \tag{1}$$

of bandwidth Ω and chirp length T that results in a proportionality between the IF signal's time axis t and the transfer function's frequency axis ω. Capital letters describing the physical signals are thus used in the following to emphasize this. The equivalence can also be seen by calculating the mixing product of the transmit signal X

$$X(t) = A_0 \cdot \cos(\omega(t) \cdot t + \phi_0) \tag{2}$$

having the amplitude A_0 and the phase ϕ_0, and the receive signal Y, which is basically scaled in the amplitude and the time as well as phase-shifted

$$\begin{aligned} Y(t) &= \Re\{A_0 \cdot \cos(\omega(t) \cdot t + \phi_0) * \underline{h}\} \\ &= A_0 \cdot \sum_{n=0}^{\infty} |a_n| \cos(\omega(t) \cdot t + \omega(t)\tau_n + \phi_n + \phi_0) \end{aligned} \tag{3}$$

by the several components n of the transfer function $\underline{H}$ or the impulse response $\underline{h}$, respectively. $\underline{a}_n$ and τ_n denote the amplitudes and delay times of the reflection components in $\underline{H}$ and $\underline{h}$

$$\underline{H}(j\omega) = \sum_{n=0}^{\infty} \underline{a}_n e^{j\omega\tau_n} \quad \text{or} \quad \underline{h}(\tau) = \sum_{n=0}^{\infty} \underline{a}_n \delta(\tau - \tau_n). \tag{4}$$

Due to the low-pass filter in the IF path, denoted in (5) by the bar, it can be seen that the mixing product S is equal to the real part of the transfer function

$$\begin{aligned} S(t) &= \overline{X(t) \cdot Y(t)} \\ &= \frac{A_0^2}{2} \cdot \sum_{n=0}^{\infty} |a_n| \cos(\omega(t)\tau_n + \phi_n) \\ &= \frac{A_0^2}{2} \cdot \Re\{\underline{H}(\omega(t))\}. \end{aligned} \tag{5}$$

Thus, it is shown that a frequency-domain measurement of the transfer function is obtained by the FMCW pulse. The spectrum of this signal, calculated, e.g., by the discrete Fourier transform, thus resembles the radar impulse response $\underline{h}(\tau)$. Lower case letters are, in the following, used to describe the physical values that operate on the fast time axis τ.

B. Calibration

The error model $\underline{\mathbf{R}}$ is now introduced as a 2-port matrix to include the effects of linear systematic errors on the measurement. This approach is commonly used in VNA calibration [8] and covers mismatches between the device ports, conversion losses in the mixing stages, and also free-space propagation losses [7] among other linear errors. The error network transforms the ideal incident and reflected power waves $\underline{X}$ and $\underline{Y}$ at the measurement object to the values $\underline{\tilde{X}}$ and $\underline{\tilde{Y}}$ that are now containing systematic errors and are seen by the ideal measurement port. The relationship between the ideal transfer function $\underline{H}$ and the error-prone transfer function $\underline{\tilde{H}}$ at the sensor is given by

$$\underline{\tilde{H}} = \underline{R}_{11} + \frac{\underline{R}_{12}\underline{R}_{21}\underline{H}}{1 - \underline{R}_{22}\underline{H}}. \tag{6}$$

There are three error terms: the input mismatch $\underline{R}_{11}$, the product of the transmission terms $\underline{R}_{12}\underline{R}_{21}$, and the output mismatch $\underline{R}_{22}$ that have to be known to remove the influence of the error network by means of calibration, as can be seen from (6). In VNA calibration topics, this is commonly very well-known as 3-term calibration. In the context of FMCW radar calibration, an additional problem is the loss of information about the imaginary part of (6), since (5) has to be applied to describe the measurement signal.

Since the measured transfer function is related to a physical system, it has to be causal. Therefore, to calibrate the FMCW sensor, a Hilbert transformation $\mathcal{H}\{\cdot\}$ has to be applied on the IF signal $S(t)$. The corresponding analytic signal can then be obtained by

$$\underline{S}(t) = \mathcal{H}\{S(t)\} = \text{IDFT}\{\text{DFT}\{S(t)\} \cdot \text{step}(\omega)\} \tag{7}$$

where step(ω) is the Heaviside unit step function.

When applying the Hilbert transformation this way, sidelobes from the complex conjugated left part ($\omega < 0$) of the IF signal's spectrum that reach into the domain $\omega > 0$ may introduce errors to the analytic signal. The largest contributors to this kind of distortion are reflections that occur as input mismatches at internal points in the measurement system, and thus appear close to $\omega = 0$, which is equivalent to $\tau = 0$. Due to this reason, we propose to compensate only for the real part $\Re\{\underline{R}_{11}\}$ by performing a match measurement.

Fig. 2. Photograph of the measurement setup showing the radar sensor on the left-hand side and the sample holder on the right-hand side on an optical rail.

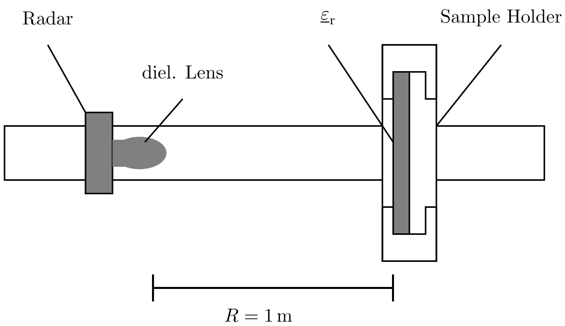

Fig. 3. Schematic of the measurement setup according to Fig. 2. The distance between the dielectric lens surface and the sample surface is approximately 1 m.

Furthermore, two additional reflection measurements are needed for a complete calibration scheme. For this purpose, we propose a short and a line calibration standard. It can be seen from (6) that all the remaining error components of $\underline{\mathbf{R}}$ are modulations on the target's transfer function and cannot occur closer to the sensor as the target itself. The formulation of all calibration measurements is summarized in

$$\text{Match}: \quad S_{\text{match}} = \Re\{\underline{R}_{11}\} \tag{8}$$

$$\text{Short}: \quad S_{\text{short}} - S_{\text{match}} = \Re\left\{-\frac{\underline{R}_{12}\underline{R}_{21}}{1+\underline{R}_{22}}\right\} \tag{9}$$

$$\text{Line}: \quad S_{\text{line}} - S_{\text{match}} = \Re\left\{\frac{\underline{R}_{12}\underline{R}_{21}\underline{H}_{\text{line}}}{1-\underline{R}_{22}\underline{H}_{\text{line}}}\right\}. \tag{10}$$

The line standard of length Δl in (10) is described by $\underline{H}_{\text{line}} = -1 \cdot \exp(j2\omega\Delta l c_0^{-1})$. After the calculation of the three error terms from the calibration measurements [8], the additional MUT measurement can then be corrected by

$$\underline{H}_{\text{MUT}} = \frac{\mathcal{H}\{S_{\text{MUT}} - S_{\text{match}}\}}{\underline{R}_{12}\underline{R}_{21} + \underline{R}_{22}\mathcal{H}\{S_{\text{MUT}} - S_{\text{match}}\}}. \tag{11}$$

Thus, it has been shown that an error-corrected measurement of the MUT's complex transfer function is possible by applying the proposed calibration methodology. The calibration also results in a shift of the phase reference plane into the measurement plane.

III. Measurement Setup

This section presents the design of the used measurement setups alongside the execution of the calibration. The functionality of the previously described calibration method is shown by the first measurements in both the measurement setups. A mm-wave radar sensor [12] operating from 200 to 250 GHz is utilized in both the setups. The radar system is based on a silicon–germanium (SiGe) monolithic microwave integrated circuit (MMIC), which is fabricated in Infineon's B11HFC BiCMOS technology. The phase-lock loop-stabilized voltage-controlled oscillator (VCO) operates from 100 to 125 GHz and is doubled in frequency in order to provide an RF source at the aforementioned frequency range. The MMIC features integrated on-chip antennas, since the RF-signal coupling using bond wires is not feasible at these high frequencies. Furthermore, two separate antennas for transmitting and receiving are used in order to increase the isolation between the transmit and the receive path. Differentially fed patch antennas are used in both the paths. The ramp duration for a measurement over the complete bandwidth can be chosen between 1 and 16 ms. The IF signal is processed according to the methodology in Section II.

A. Collimating Lens Setup

The first considered setup, which is shown in Figs. 2 and 3, uses a collimating lens to achieve plane phase fronts directly in front of the antenna. The collimating behavior corresponds to a very high antenna gain of 55.8 dBi when considering the transmit and the receive behavior in total. The corresponding 3-dB opening angle is 3.35°. The utilized lens is made from polytetrafluoroethylene (PTFE, Teflon) to achieve low losses and only weak surface reflections. It is elliptically shaped in order to refract the circular wavefronts, which are radiated by the patches, to plane wavefronts in the surrounding environment [13]. The diameter of the antenna 3-dB footprint on the material sample can be calculated to 5.85 cm. The edge length of the square material sample is chosen to 30 cm to ensure that diffraction at the sample edges or fringing effects do not have to be considered.

A schematic of the calibration measurements' realization is given in Figs. 4–6. The corresponding radar echo profile of the match measurement is presented in Fig. 7. It is shown alongside the echo profile of the short and line measurements after subtracting the match according to (8) and (10). The additional line measurement does not significantly differ from the short's echo profile, except the very narrow shift of approximately 200 μm. Since the mechanical movement can be a source of errors in calibration, the authors want to stress the fact that the exact shift length can be extracted from the radar measurement. The pulse shape of the target reflection in **S**HORT and **L**INE standard measurements does not change, because the transmission behavior of the error model $\underline{\mathbf{R}}$ is not altered. The detection of the differential shift between the **S**HORT and **L**INE peaks at approximately 0.8 m in Fig. 7 can be expressed as a deconvolution of these impulse response components. The deconvolution of this reflection component then corresponds to a division of the nominators from (8) and (10). In this case, the exact line length is calculated to 205.3 μm.

After the error model is extracted from the aforementioned three measurements, another measurement of the **M**ATCH

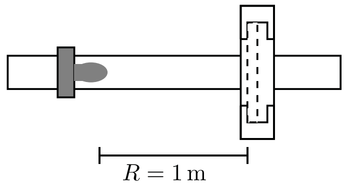

Fig. 4. Schematic of the match measurement without a target in the measurement plane.

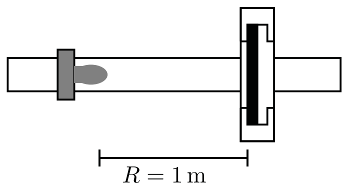

Fig. 5. Schematic of the short measurement with a metallic plate target.

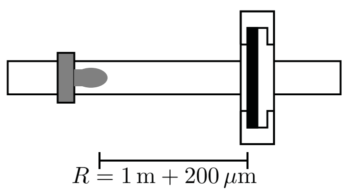

Fig. 6. Schematic of the line measurement with a metallic plate target that is precisely shifted in comparison with the short measurement.

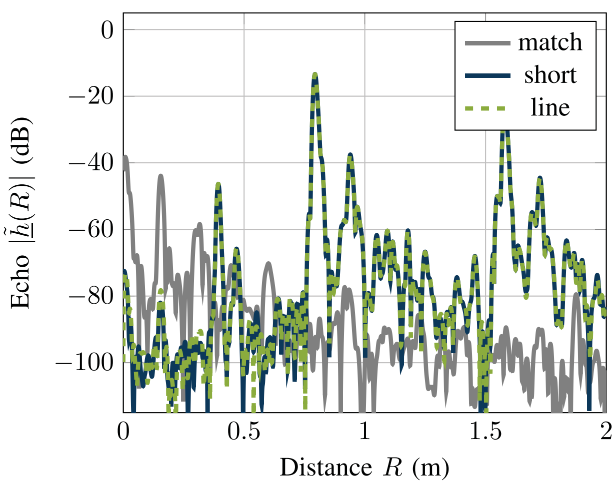

Fig. 7. Radar echo profiles of the calibration measurements in the collimating lens setup.

and **S**HORT standards is executed. This allows estimating the dynamic measurement range of the system. Fig. 8 shows the frequency-domain results from these measurements in a VNA comparable form. The magnitude of the **M**ATCH measurement reveals that the lower boundary of the measurement range is approximately between −30 and −40 dB. The magnitude of the **S**HORT reflection factor is expected to be constant at 0 dB, and from Fig. 8, it can be seen that the variation is in between ±0.4 dB.

B. Focusing Mirror Setup

An alternative measurement setup is presented in order to increase the dynamic range of the measurement system. Due to

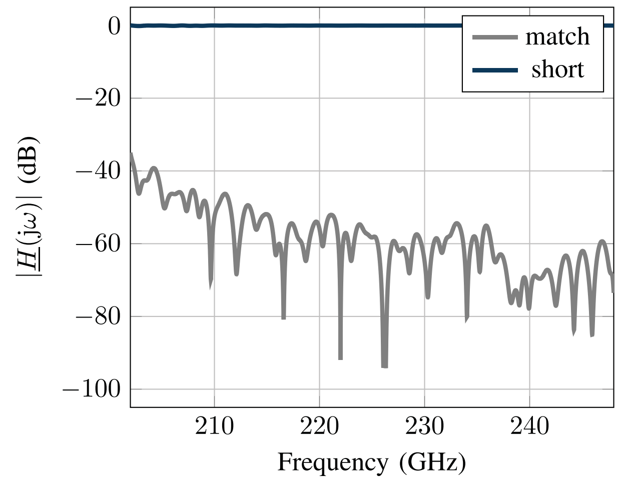

Fig. 8. Visualization of the collimating lens setups' dynamic range obtained by a second measurement using the calibration standards **S**HORT and **M**ATCH.

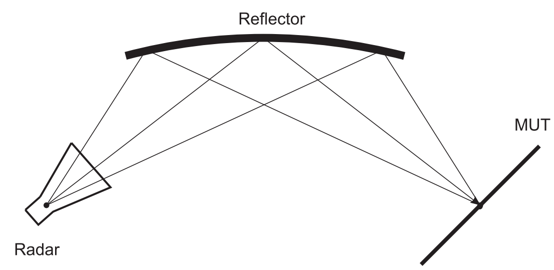

Fig. 9. Schematic of the measurement setup showing the radar sensor on the left-hand side and the sample holder on the right-hand side with the elliptical mirror in the center.

the dielectric lens, which has been used before, the target pulse at 0.8 m in Fig. 7 is usually followed by additional multiple reflections inside the dielectric lens (up to 1.3 m). Sidelobes from these reflections may overlap with the target pulse and distort the measurement. In frequency domain representation, they appear as an additional oscillation, which modulates the measured signal. To increase the performance of the measurement setup, a metallic mirror with an ellipsoid surface is used. A schematic of the new setup is presented in Fig. 9. In this setup, the on-chip antenna is placed in one of the mirrors' focal points, whereas the material sample is placed in the second focal point. Since all focal rays inside an ellipsoid are reflected into the other focus, a very precise measurement can be achieved.

A full 3-D electromagnetic simulation using the Integral Equation Solver of CST Microwave Studio has been done to investigate the focusing performance of this setup. To this purpose, the on-chip antenna simulation from [12] has been embedded into a larger simulation environment including the mirror. Fig. 10 shows the logarithmic magnitude of the electric field at the center frequency of 225 GHz. The beam waist at the focal point is approximately 1 cm in diameter and is, thus, much smaller than in the previously discussed collimating lens scenario. The calibration procedure of the measurement setup is similar to the one presented in Figs. 4–6. Consecutively, an empty sample holder, a metallic plate, and a shifted version

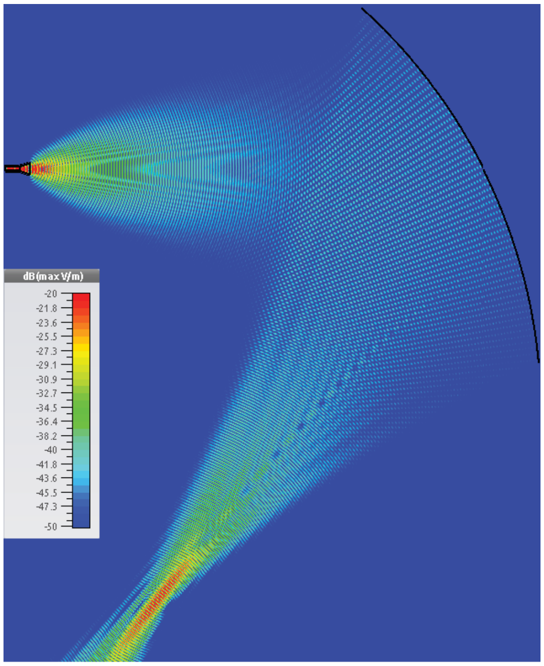

Fig. 10. Simulated z-component of the electric field in the focusing mirror setup at 225 GHz, showing the antenna in the top-left corner, the mirror in the top-right corner, and the focal point in the bottom-left corner, where the MUT will be placed.

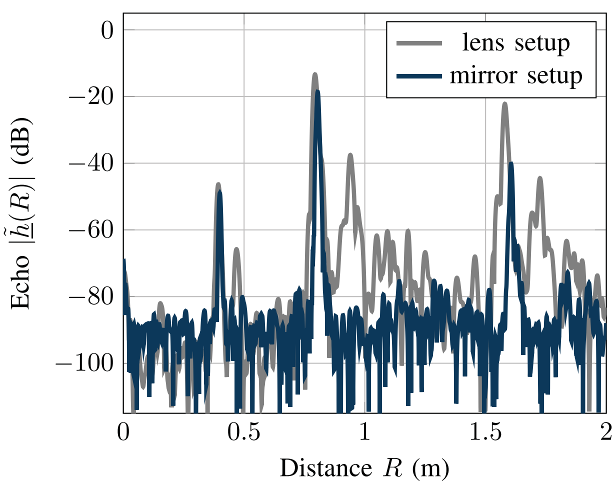

Fig. 11. Comparison between the short measurements of both the setups after subtracting the match measurement.

of the same plate are measured, before the material sample can be placed in the sample holder. Fig. 11 shows the radar echo profiles of the short measurements of both the setups after subtracting the according match results. This allows comparing the performances of both the setups. It can be clearly seen that the impulse response of the target is much clearer in the mirror-based setup than in the lens-based setup, since multiple reflections between the mirror and the on-chip antenna are geometrically not possible. Thus, a much better separation of the target pulse is possible, which increases the measurement's accuracy.

An estimation of the dynamic measurement range of the mirror setup is presented in Fig. 12, which can be compared with Fig. 8. The figure shows that the dynamic range can be

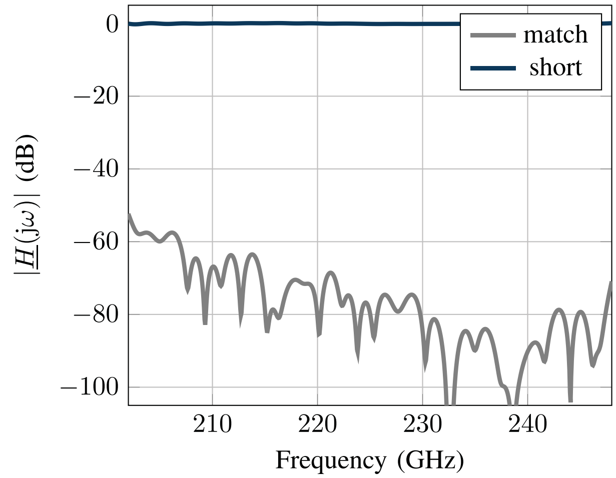

Fig. 12. Visualization of the focusing mirror setup's dynamic range obtained by a second measurement using the calibration standards **S**HORT and **M**ATCH. The dynamic range is increased by approximately 20 dB when compared with Fig. 8.

increased by approximately 20 dB over the entire frequency range. The systematic components, which result from the sidelobes of multiple reflections in the collimating lens setup, limit the measurement range. The repetition of the **S**HORT measurement also reveals a lower ripple of only ± 0.1 dB. Thus, the discussed results presume that the mirror-based setups allows even more precise material characterization measurements.

IV. Material Characterization

In order to extract the material parameters, dielectric constant ε_r, losses $\tan_\delta$, and material thickness d, an optimization problem has to be solved. The cost function that has to be minimized is derived from the least squares fitting between the measurement data and the analytic model for a dielectric slab of finite thickness [14]. The reflection factor $\underline{\Gamma}$ that is calculated from [14] is a function of frequency, dielectric properties, incident angle, and also thickness. Due to the mechanical alignment of the setup, the incident angle is very stable at 0° and does not need any error correction. An offset distance l_{offset} between the calibration plane and the material sample that results from finite stiffness of the MUT sample has to be estimated during the optimization process in addition to the remaining three material parameters (rel. permittivity, losses, and thickness). This is used to compensate for additional phase rotations due to minimal additional distance, with respect to the short position, in front of the sample. The cost function can then be stated as follows:

$$\varepsilon_r, \tan_\delta, d, l_{\text{offset}} = \operatorname{argmin} |\underline{\Gamma}(f, \varepsilon_r, \tan_\delta, d, l_{\text{offset}}) - \underline{\Gamma}_{\text{meas}}(f)|. \quad (12)$$

For the functions' four parameters, initial values are handed over to the parameter extraction algorithm. The precise calculation of the material properties is then iteratively performed by a Gauss–Newton implementation. To this purpose, the function's Jacobi-Matrix $\mathbf{J}$ is calculated numerically by finite differences. The Jacobi-Matrix is of size $[F \times 4]$, where

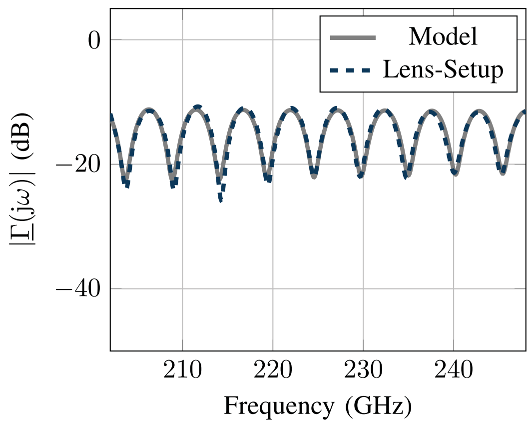

Fig. 13. Measured (lens setup) reflection factors of a PTFE (Teflon) sample compared with the extracted model.

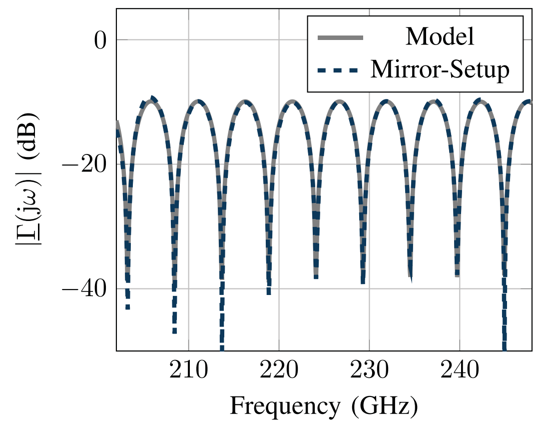

Fig. 14. Measured (mirror setup) reflection factors of a PTFE (Teflon) sample compared with the extracted model.

F is the number of frequency samples. A least squares solution is found by solving the linear equation system

$$(\mathbf{J}^T \cdot \mathbf{J})\vec{x} = \mathbf{J}^T \cdot \vec{r}. \tag{13}$$

In (13), $\vec{x}$ is the $[4 \times 1]$ vector containing the four optimization parameters and $\vec{r}$ is a $[F \times 1]$ vector of all frequency samples. The entries of $\vec{r}$ correspond to the residual differences between the model and measurement of (12). A least squares' solution is found by the additional multiplication of the overdetermined original system by $\mathbf{J}^T$.

Problems may occur in finding a solution in the linear equation system of (13), since the entries in the columns of $\mathbf{J}$ corresponding to d and l_{offset} are much larger than the entries belonging to ε_r and $\tan_\delta$. Thus, the matrix $(\mathbf{J}^T \cdot \mathbf{J})$ is very likely to be ill-conditioned. To cope with that problem, the authors propose to use a Tychonov-regularization based on the variances in the Jacobi-Matrix's columns. The regularized system is formulated to

$$(\mathbf{J}^T \cdot \mathbf{J} + \operatorname{diag}(\vec{\sigma}^{\,-2}))\vec{x} = \mathbf{J}^T \cdot \vec{r} \tag{14}$$

where $\vec{\sigma}^{\,-2}$ is the $[1 \times 4]$ vector of the 1 over the variances corresponding to each column of $\mathbf{J}$. Using these parameters, a solution is found after 10–20 iterations.

Figs. 13 and 14 show the calibrated reflection coefficients of a PTFE (Teflon) sample of 20-cm thickness. The plots show that the resonating behavior due to the finite sample thickness is very well captured by both the measurements. From these results, the material properties are extracted according to the steps from (12) to (14). In Figs. 13 and 14, the functions of the modeled reflection coefficients, based on the least squares fits resulting from both the setups, are also shown. It can be seen that the mirror-based measurement setup reveals a much higher dynamic range, as was already expected by the calibration measurements in Figs. 8 and 12. Due to the lower dynamic range in the lens-based measurements, the material samples tend to appear more lossy, since the minimum level of the reflection factors at resonance is mainly influenced by material losses.

An overview of the extracted parameters of all considered material samples for both the setups is given in Tables I and II. The considered material samples include well-known materials for which references are available in literature, such as Teflon [15], polypropylene (PP) [16], polyoxymethylene (POM) [17], PVC [17], and acrylic glass [polymethyl-methacrylate (PMMA)] [16]. Additionally, polylactide (PLA), a common 3-D printer material, is characterized. Since 3-D printers allow manufacturing with different filling levels, the results for this material are further subdivided into 50% filling and 100% filling. Furthermore, black (B) and also white (W) colored PLA is characterized. The obtained results agree very well with literature for both the setups, which are summarized in Table III. The larger deviation from literature for PLA is explained by the much higher center frequency in these setups. The mirror-based setup achieves a higher accuracy, due to the larger dynamic range, than the lens setup, which is in turn much simpler and more robust. The main differences in the material parameter extraction between both the setups occur at the extraction of the loss tangent. The results for the relative permittivity are very similar in both the measurements and agree with literature values. The fitting curves for all the materials agree with the measured

TABLE I
MATERIAL CHARACTERIZATION RESULTS FROM LENS SETUP

Material	Thickness	rel. Perm.	$\tan_\delta$	Offset
PTFE	20.04 cm	1.99	1.0E−3	974 µm
PP	19.83 cm	2.22	8.3E−3	−981 µm
POM	13.05 cm	3.14	6.4E−2	197 µm
PVC	14.75 cm	2.62	1.8E−1	−183 µm
PMMA	11.92 cm	2.33	1.6E−2	342 µm
PLA (B,50%)	5.09 cm	2.41	8.8E−2	501 µm
PLA (B,100%)	5.01 cm	2.56	1.1E−1	367 µm
PLA (W,100%)	5.04 cm	2.56	1.0E−1	263 µm

TABLE II
MATERIAL CHARACTERIZATION RESULTS FROM MIRROR SETUP

Material	Thickness	rel. Perm.	$\tan_\delta$	Offset
PTFE	20.03 cm	2.02	4.3E−4	−864 µm
PP	19.71 cm	2.20	4.7E−3	385 µm
POM	12.98 cm	3.13	1.5E−2	142 µm
PVC	14.84 cm	2.65	1.4E−1	−143 µm
PMMA	11.73 cm	2.33	1.5E−2	−159 µm
PLA (B,50%)	5.07 cm	2.51	1.6E−2	−156 µm
PLA (B,100%)	4.92 cm	2.65	2.6E−2	−163 µm
PLA (W,100%)	4.95 cm	2.65	2.2E−2	130 µm

TABLE III
REFERENCE VALUES FROM LITERATURE

Material	rel. Perm.	$\tan_\delta$	rel. Deviation
PTFE	2.07	1E−4	2.4%
PP	2.25	3.6E−3	2.2%
POM	3.1	1.6E−2	0.9%
PVC	2.7	1.1E−2	1.9%
PMMA	2.6	1.2E−2	10%
PLA (@ 10 GHz)	3.5	1.6E−2	24%

curves as well, as can also be seen from the results for Teflon in Figs. 13 and 14. The misalignment between the calibration plane and the material sample surface, which is expressed by the offset term, is also very small in all the measurements, showing a high precision of the measurement setups and the well-working calibration methodology.

V. CONCLUSION

In this paper, we presented a calibration method for FMCW radar transceivers operating in the mm-wave bands between 200 and 250 GHz. To this purpose, algorithms from vector network analysis are adapted and extended to the special properties of FMCW systems. Based on the presented methods, a calibration using three simple measurements can be achieved. The calibrated transceivers are furthermore used to extract the extrinsic material properties of different dielectric materials such as Teflon or PLA. The extraction method is based on an optimization problem to minimize the differences between an analytic reflection factor model and the measurement results from two different setups. The first setup is based on a collimating lens, which allows illuminating the material sample with plane phase-fronts very close to the lens surface. In the second setup, an elliptical mirror is used to achieve a focal point in the measurement plane. The measurements have shown that the elliptical mirror setup has a higher dynamic range because of less multiple reflections in the measurement setup. Eventually, the material parameters for different frequently used materials were extracted from both the setups. The obtained results are comparable with each other and with available literature values, as well.

REFERENCES

[1] M. Vogt, C. Schulz, C. Dahl, I. Rolfes, and M. Gerding, "An 80 GHz radar level measurement system with dielectric lens antenna," in *Proc. 16th Int. Radar Symp.*, Jun. 2015, pp. 712–717.

[2] C. Baer, T. Jaeschke, N. Pohl, and T. Musch, "Contactless detection of state parameter fluctuations of gaseous media based on an mm-wave FMCW radar," *IEEE Trans. Instrum. Meas.*, vol. 64, no. 4, pp. 865–872, Apr. 2015.

[3] M. Mallach and T. Musch, "Towards a fast microwave tomography system for multiphase flow imaging," in *Proc. IEEE Int. Instrum. Meas. Tech. Conf.*, May 2017, pp. 1–6.

[4] S. Nowok, S. Kueppers, H. Cetinkaya, M. Schroeder, and R. Herschel, "Millimeter wave radar for high resolution 3D near field imaging for robotics and security scans," in *Proc. Int. Radar Symp.*, Jun. 2017, pp. 1–10.

[5] Y. S. Koo, L. Ren, Y. Wang, and A. E. Fathy, "UWB microdoppler radar for human gait analysis, tracking more than one person, and vital sign detection of moving persons," in *IEEE MTT-S Int. Microw. Symp. Dig.*, Jun. 2013, pp. 1–4.

[6] I. Vakili, L. Ohlsson, L.-E. Wernersson, and M. Gustafsson, "Time-domain system for millimeter-wave material characterization," *IEEE Trans. Microw. Theory Techn.*, vol. 63, no. 9, pp. 2915–2922, Sep. 2015.

[7] J. W. Schultz, *Focused Beam Methods: Measuring Microwave Materials in Free Space*. Scotts Valley, CA, USA: CreateSpace Independent, 2012.

[8] N. Shoaib, *Vector Network Analyzer (VNA) Measurements and Uncertainty Assessment* (PoliTO Springer Series). Cham, Switzerland: Springer, 2016.

[9] J. Barowski and I. Rolfes, "Ellipsometry based on millimeter wave radar measurements," in *Proc. Eur. Microw. Conf.*, Oct. 2017, pp. 934–937.

[10] J. Barowski and I. Rolfes, "Millimeter wave material characterization using FMCW-transceivers," in *Proc. 2nd IEEE Int. Microw. Workshop Ser. Adv. Mater. Process.*, Sep. 2017, pp. 1–3.

[11] T. Hauschild and R. Knochel, "Calibration of short range FMCW-radars with network analyzer calibration techniques," in *IEEE MTT-S Int. Microw. Symp. Dig.*, vol. 2, Jun. 1998, pp. 969–972.

[12] S. Thomas, C. Bredendiek, T. Jaeschke, F. Vogelsang, and N. Pohl, "A compact, energy-efficient 240 GHz FMCW radar sensor with high modulation bandwidth," in *Proc. German Microw. Conf.*, Mar. 2016, pp. 397–400.

[13] N. Pohl, T. Jaeschke, and M. Vogt, "An SiGe-chip-based 80 GHz FMCW-radar system with 25 GHz bandwidth for high resolution imaging," in *Proc. 14th Int. Radar Symp.*, vol. 1, Jun. 2013, pp. 239–244.

[14] W. Burside and K. Burgener, "High frequency scattering by a thin lossless dielectric slab," *IEEE Trans. Antennas Propag.*, vol. AP-31, no. 1, pp. 104–110, Jan. 1983.

[15] T. Zwick, A. Chandrasekhar, C. W. Baks, U. R. Pfeiffer, S. Brebels, and B. P. Gaucher, "Determination of the complex permittivity of packaging materials at millimeter-wave frequencies," *IEEE Trans. Microw. Theory Techn.*, vol. 54, no. 3, pp. 1001–1010, Mar. 2006.

[16] M. N. Afsar, "Precision millimeter-wave measurements of complex refractive index, complex dielectric permittivity, and loss tangent of common polymers," *IEEE Trans. Instrum. Meas.*, vol. IM-36, no. 2, pp. 530–536, Jun. 1987.

[17] A. Elhawil, L. Zhang, J. Stiens, and R. Vounckx, "A quasi-optical free-space method for dielectric constant characterization of polymer materials in mm-wave band," in *Proc. Symp. IEEE/LEOS Benelux Chapter*, Jun. 2007, pp. 187–190.

Jan Barowski (S'12–M'18) was born in Bochum, Germany, in 1988. He received the B.Sc., M.Sc., and Dr.Ing. degrees in electrical engineering from Ruhr University Bochum, Bochum, in 2010, 2012, and 2017, respectively.

Since 2012, he has been with the Institute of Microwave Systems, Ruhr University Bochum, as a Research Assistant. His current research interests include radar signal processing, radar imaging, and material characterization techniques.

Marc Zimmermanns was born in Wuppertal, Germany, in 1986. He received the M.Sc. degree in electrical engineering and information technology from Ruhr University Bochum, Bochum, Germany, in 2012, where he is currently pursuing the Ph.D. degree in electrical engineering.

Since 2012, he has been a Research Assistant with the Institute of Microwave Systems, Ruhr University Bochum. His current research interests include multiport calibration methods and material characterization.

Ilona Rolfes (M'06) received the Dipl.Ing. and Dr.Ing. degrees in electrical engineering from Ruhr University Bochum, Bochum, Germany, in 1997 and 2002, respectively.

From 1997 to 2005, she was with the High Frequency Measurements Research Group, Ruhr University Bochum, as a Research Assistant. From 2005 to 2009, she was a Junior Professor with the Department of Electrical Engineering, Leibniz Universitäet Hannover, Hannover, Germany, where she became the Head of the Institute of Radiofrequency and Microwave Engineering in 2006. Since 2010, she has been leading the Institute of Microwave Systems, Ruhr University Bochum. Her current research interests include high-frequency measurement methods for vector network analysis, material characterization, noise characterization of microwave devices, sensor principles for radar systems, and wireless solutions for communication systems.